Stationary states of forced two-phase turbulence

By S. S. Jain AND A. Elnahhas

1. Motivation and objectives

The deformation, fragmentation, and coalescence of bubbles and droplets in a turbulent environment is an important problem in various environmental and industrial settings (Jain 2017; Ni 2024). In the atmosphere, the enhanced efficiency of water droplet collision–coalescence events due to air turbulence heavily influences cloud formation and warm rain initiation (Grabowski & Wang 2013). At the ocean–atmosphere interface, underwater turbulence generated due to breaking waves breaks apart large entrained air pockets into smaller bubbles, facilitating mass transfer between the ocean and the atmosphere (Dieke 2022). Finally, turbulent emulsions, i.e., a homogenized mixture of two fluids of similar densities, are ubiquitously formed for use in pharmaceutical and industrial processing (Wang *et al.* 2007; Kilpatrick 2012). As such, an understanding of how turbulence influences (and is influenced by) the dispersed phase, as parameters such as density and viscosity ratios between the carrier and dispersed phases, as well as the volume fraction occupied by the dispersed phase, are varied, is of paramount importance to understanding these ubiquitous flows.

While these examples contain irreducible effects due to anisotropy and large-scale shear, the simplest setup to study the essential physics of deformation, fragmentation, and coalescence of bubbles and droplets in a turbulent environment is homogeneous isotropic turbulence (HIT). In this setup, the dynamics and statistics of droplets and bubbles, both larger and smaller than the Hinze scale, the scale at which inertial forces due to turbulence causing fragmentation are balanced by the restorative force of the surface tension, can be studied in the absence of large-scale anisotropy. Recent studies that utilize two-phase HIT as a testbed can be broken down into two categories: The first category considers the detailed dynamics of individual bubbles and emulsions during the first few breakup events, characterizing and quantifying things such as the generation of sub-Hinze scale bubbles due to rapid successive breakup events and capillary fragmentation (Riviére *et al.* 2021, 2022), the effect of eddies far away from the two-phase interface on the deformation process (Vela-Martín & Avila 2021), bubble deformation modes due to turbulent fluctuations (Perrard *et al.* 2021), the non-vanishing probability of breakup at sub-Hinze scales due to increasingly intermittent turbulent fluctuations (Vela-Martín & Avila 2022), and the role of the viscosity ratio between the two phases on the rate of bubble breakup and the critical Weber number at which they break (Farsoiya *et al.* 2023). The second category considers characterizing the statistical properties of numerous bubbles and droplets present simultaneously in a turbulent environment. Within this category, Dodd & Ferrante (2016) studied the turbulent kinetic energy (TKE) budgets of droplets at various density ratios within decaying HIT. Crialesi-Esposito *et al.* (2022, 2023) studied the influence of viscosity ratios and volume fractions of the dispersed phase at unity density ratios in a forced HIT setting on the scale-by-scale energy budgets while linking the droplet-size distribution (DSD) to the local dissipation rate of turbulence, once again highlighting the importance of intermittency in the breakup dynamics. Finally,

Begemann *et al.* (2022) and Krzeczek *et al.* (2022) utilize a linear forcing approach to study the segregation properties of emulsions, highlighting that even minor variations in the density ratio of the two phases from slightly below to slightly above unity shifts the DSD to have fewer super-Hinze bubbles and more sub-Hinze scale drops.

In all the aforementioned studies, decaying turbulence cases are utilized considerably. However, the initial velocity fields inside the dispersed phase are somewhat arbitrarily chosen as zero. It is unclear whether this affects the breakup statistics, as no systematic study of the effect of the internal initial condition on the breakup statistics has been performed. To overcome this ambiguity, it would be best to characterize the breakup dynamics at a statistically stationary state, where individual events can be tracked. To achieve this state, forcing is necessary to sustain the continuously dissipating turbulence, ensuring that the turbulence properties do not change during the breakup processes. In the cases where forcing has been used, both simultaneous (both phases) and single-phase, linear, physical-space forcing have been utilized in various studies (Lundgren 2003; Rosales & Meneveau 2005). However, single-phase (carrier) forcing is only used for the cases that study single bubbles in HIT (Riviére *et al.* 2021, 2022), while simultaneous mixture-phase (both phases) forcing has been applied only to density ratios representative of emulsions (Begemann *et al.* 2022; Crialesi-Esposito *et al.* 2022; Krzeczek *et al.* 2022; Crialesi-Esposito *et al.* 2023). As such, there remain open questions concerning the differing effects of simultaneous mixture-phase (both phases) forcing and single-phase (carrier) forcing, as well as how the aggregate properties of the two-phase HIT vary with density ratio when forced.

In this work, we perform forced numerical simulations of two-phase HIT. This study will primarily belong to the second category in the classification of existing studies above. We formulate various forcing schemes, including mixture-phase and single-carrier-phase forcing for two-phase turbulent flows combined with proportional controllers (Bassenne *et al.* 2016), and use them to characterize the aggregate statistical properties of stationary two-phase turbulence with non-unity density ratios, representing suspended heavier drops in turbulence, lighter bubbles in turbulence, and turbulent emulsions. We study these global aggregate statistics by varying density ratio, void fraction, and Weber number. These aggregate statistics will help in the understanding of the global behavior of the two-phase mixture and will influence future choices in designing cases to probe the more detailed dynamics of the two-phase turbulent breakup problem. This study will also aid in the development of subgrid-scale models for larger-scale simulations of two-phase turbulent flows.

The rest of the report is structured as follows: Section 2 presents the governing equations, numerical scheme, the two-phase global energetic equations, formulations of the various tested forcing schemes, and the computational setup. Section 3 presents results on the variation of the energy of each phase as non-dimensional parameters such as void fraction, density ratio, and large-scale Weber number are varied for various forcing schemes. We also discuss the use of filtering to extract the spectrum of a two-phase flow, and report the effect of void fraction on the spectrum of both phases. Furthermore, the variation of DSD as a function of large-scale Weber number is discussed for forced emulsions. Finally, a summary of the findings and concluding remarks are presented in Section 4.

2. Methodology

2.1. *Governing equations and numerical methods*

In this work, we consider incompressible two-fluid flows. A phase-field/diffuse-interface method is used as an interface-capturing method. The details of the formulation are presented in the following subsections.

2.1.1. *Phase-field model*

In this method, the volume fraction of one of the fluids is indicated by the phase-field variable $\phi = \phi_1$, which satisfies the relation $\sum_{l=1,2} \phi_l{=}1$ by definition, where the subscript l denotes phase index. Then, the accurate conservative diffuse-interface (ACDI) model for ϕ (Jain 2022) can be written as

$$\frac{\partial \phi}{\partial t} + \vec{\nabla} \cdot (\phi \vec{u}) = \vec{\nabla} \cdot \left\{ \Gamma \left\{ \epsilon \vec{\nabla} \phi - \frac{1}{4} \left[1 - \tanh^2 \left(\frac{\psi}{2\epsilon} \right) \right] \frac{\vec{\nabla} \psi}{|\vec{\nabla} \psi|} \right\} \right\}, \tag{2.1}$$

where $\vec{u}$ is the velocity, Γ denotes the velocity-scale parameter, and ϵ is the interface thickness scale parameter. Here, ψ is an auxiliary variable and represents the signed-distance-like function from the interface, which is defined as

$$\psi = \epsilon \ln \left(\frac{\phi + \varepsilon}{1 - \phi + \varepsilon} \right). \tag{2.2}$$

Note that a small number ε is added to both the numerator and denominator to avoid division by 0, and ε is chosen as $\varepsilon = 10^{-100}$. The right-hand-side (RHS) term of Eq. (2.1) is the interface-regularization term, which is an artificial term that is added to maintain the constant thickness of the interface. The interface-regularization term contains a diffusion and a sharpening term, which balance each other to maintain a constant interface thickness on the order of ϵ. The ACDI model is discretized using a second-order skew-symmetric split central discretization (Jain & Moin 2022).

Jain (2022) showed that ϕ remains bounded between 0 and 1 using a central scheme, provided $\Gamma/|\vec{u}|_{max} \geq 1$ and $\epsilon/\Delta > 0.5$ conditions are met, where Δ represents the grid size. Therefore, in this work, $\Gamma/|\vec{u}|_{max} = 1$ and $\epsilon/\Delta = 0.51$ are used for all the simulations.

The recently developed ACDI method (Jain 2022) has been shown to be suitable for complex turbulent flow simulations (Jain 2022; Hwang & Jain 2023) and a wide range of other multiphysics flow problems (Collis *et al.* 2022; Scapin *et al.* 2022; Brown *et al.* 2023; Jain 2023). It is known to be more accurate than other existing phase-field models because it maintains a sharper interface (with only one-to-two grid points across the interface) while being non-dissipative, robust, less expensive, and conservative (without the need for any geometric treatment). Because of these advantages, the ACDI method is chosen as the interface-capturing method in this work.

2.1.2. *Momentum equation*

Furthermore, the effect of the interface-regularization term on the RHS of Eq. (2.1) is considered in the momentum equation as

$$\frac{\partial \rho u_i}{\partial t} + \frac{\partial \rho u_i u_j}{\partial x_j} = -\frac{\partial p}{\partial x_i} + \frac{\partial \tau_{ij}}{\partial x_j} + \frac{\partial u_i f_j}{\partial x_j} + \sigma \kappa \frac{\partial \phi_1}{\partial x_i}, \tag{2.3}$$

where i and j are the Einstein indices, τ_{ij} is the stress tensor expressed as $\tau_{ij} = 2\mu S_{ij} = \mu(\partial u_i/\partial x_j + \partial u_j/\partial x_i)$, p is the pressure and $\vec{f}$ is the implied artificial mass flux that can

be written as

$$\vec{f} = \left\{ (\rho_1 - \rho_2)\Gamma \left\{ \epsilon \vec{\nabla}\phi - \frac{1}{4}\left[1 - \tanh^2\left(\frac{\psi}{2\epsilon} \right) \right] \frac{\vec{\nabla}\psi}{|\vec{\nabla}\psi|} \right\} \right\}, \tag{2.4}$$

which results in global kinetic energy conservation with the ACDI model (Jain 2022).

2.1.3. *Surface tension modeling*

The surface tension forces, f_i^σ [last term in Eq. (2.3)], are modeled using a continuum-surface force (CSF) formulation (Brackbill *et al.* 1992), where σ is the surface tension coefficient and κ is the surface curvature, defined as $\kappa = -\vec{\nabla} \cdot \vec{n} = -\vec{\nabla} \cdot (\vec{\nabla}\psi/|\vec{\nabla}\psi|)$. The use of ψ to compute curvature in the surface tension force was shown in Jain (2022) to improve modeling of the surface tension force and reduce spurious currents significantly. This *improved CSF* model results in lower spurious currents compared to other existing models in the literature, including the free-energy based surface tension models. Hence, the *improved CSF* formulation is used to model surface tension forces in this work.

2.2. *Two-phase energetics*

2.2.1. *Mixture equations*

We can write the TKE equation as

$$\frac{\partial}{\partial t}\left(\rho \frac{u_i u_i}{2} \right) + \frac{\partial}{\partial x_j}\left(u_j \rho \frac{u_i u_i}{2} \right) = -\frac{\partial u_j p}{\partial x_j} + u_i f_i^\sigma + \frac{\partial u_i f_j}{\partial x_j} + \frac{\partial u_i \tau_{ij}}{\partial x_j} - \tau_{ij}\frac{\partial u_i}{\partial x_j}, \tag{2.5}$$

where u_i represents a fluctuating velocity. Averaging in space, we get the mean TKE equation

$$\frac{\partial k}{\partial t} = \Psi - \epsilon, \tag{2.6}$$

where $k = \langle \rho u_i u_i/2 \rangle$ is the TKE, $\Psi = \langle u_i f_i^\sigma \rangle$ is the surface tension power, and $\epsilon = \langle \tau_{ij}\partial u_i/\partial x_j \rangle$ is the dissipation; for all these terms, the averaging operator is defined as $\langle \cdot\cdot \rangle = \left[\int_V (\cdot\cdot) dV \right]/V$.

Similarly, we can write the mean surface energy equation (Dodd & Ferrante 2016) as

$$\frac{\partial se}{\partial t} = -\Psi, \tag{2.7}$$

where $se = \langle \sigma\delta \rangle$ is the surface energy (SE), for which δ is the local three-dimensional Dirac delta function active at the interface location (Tryggvason *et al.* 2011). If we define total energy as the sum of TKE and surface energy, then summing up Eqs. (2.6) and (2.7), we get the total energy equation

$$\frac{\partial k}{\partial t} + \frac{\partial se}{\partial t} = -\epsilon. \tag{2.8}$$

Figure 1 is a schematic illustrating the phase-mixed energy buckets available in a two-phase flow, and the energy transfer mechanisms between the buckets.

2.2.2. *Individual phase equations*

The individual phase momentum equations in a two-fluid formulation are

$$\frac{\partial \rho_k u_{i,k}}{\partial t} + \frac{\partial \rho_k u_{i,k} u_{j,k}}{\partial x_j} = -\frac{\partial p_k}{\partial x_i} + \frac{\partial \tau_{ij,k}}{\partial x_j}, \tag{2.9}$$

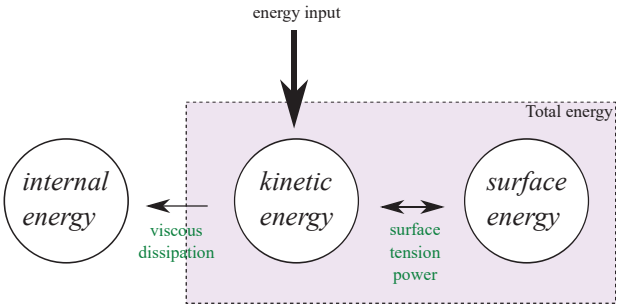

FIGURE 1. A schematic representing the different energy buckets of a multiphase flow (phases are combined) and the exchange terms between them along with energy injection point corresponding to forcing term, F_1.

where the jump condition of the stresses across the interface satisfies

$$\sum_k \left(-p_k \delta_{ij} + \tau_{ij,k}\right) n_{j,k} = \sigma \kappa n_{j,k}, \tag{2.10}$$

indicating that the balance of normal viscous and pressure forces is what contributes to surface tension forces. Then, the TKE equation for each phase k can be written as

$$\frac{\partial}{\partial t}\left(\rho_k \frac{u_{i,k}u_{i,k}}{2}\right) + \frac{\partial}{\partial x_j}\left(u_{j,k}\rho_k \frac{u_{i,k}u_{i,k}}{2}\right) + \frac{\partial u_{j,k}p_k}{\partial x_j} = \frac{\partial u_{i,k}\tau_{ij,k}}{\partial x_j} - \tau_{ij,k}\frac{\partial u_{i,k}}{\partial x_j}. \tag{2.11}$$

If we now define volume averaging within each phase k as

$$\langle \cdot\cdot \rangle_k = \frac{1}{V_k}\int_{V_k} (\cdot\cdot) dV_k = \frac{1}{V_k}\int_V (\phi_k \cdot\cdot) dV = \frac{V}{V_k}\langle \phi_k \cdot\cdot \rangle = \frac{\langle \phi_k \cdot\cdot \rangle}{\langle \phi_k \rangle},$$

and averaging in space within each phase k, we get the phase-averaged TKE equation

$$\frac{\partial k_k}{\partial t} = V_k - P_k - \epsilon_k, \tag{2.12}$$

where $k_k = \langle \phi_k \rho_k u_{i,k} u_{i,k}/2 \rangle / \langle \phi_k \rangle$ is the phase-averaged TKE, $V_k = \langle \phi_k \left(\partial u_{i,k}\tau_{ij,k}/\partial x_j\right) \rangle / \langle \phi_k \rangle$ is the phase-averaged viscous transport contribution, $P_k = \langle \phi_k \left(\partial u_{j,k} p_k/\partial x_j\right) \rangle / \langle \phi_k \rangle$ is the phase-averaged pressure transport contribution, and $\epsilon_k = \langle \phi_k \tau_{ij} \left(\partial u_i/\partial x_j\right) \rangle / \langle \phi_k \rangle$ is the dissipation of phase k [see Dodd & Ferrante (2016) for a sharp-interface formulation of phase-averaged TKE].

Figure 2 is a schematic illustrating the individual-phase energy buckets available in a two-phase flow, and the energy transfer mechanisms between the buckets.

2.3. *Forcing formulation*

To maintain the turbulent state of the flow, we can include forcing in mean TKE equation, which yields

$$\frac{\partial k}{\partial t} = \Psi - \epsilon + F_1. \tag{2.13}$$

Then the mean total energy equation is

$$\frac{\partial k}{\partial t} + \frac{\partial se}{\partial t} = -\epsilon + F_1. \tag{2.14}$$

Note, we can also force the mean surface energy equation in Eq. (2.7) by adding a nonzero force F_2. This will directly modify the energy transfer at the interface and

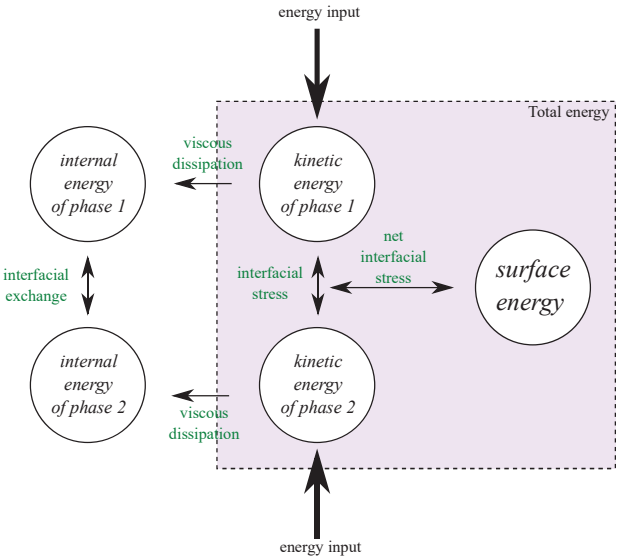

FIGURE 2. A schematic representing the different energy buckets of a two-phase flow (with the individual phases separated) and the exchange terms between them along with energy injection points corresponding to forcing terms, $F_{3,k}$.

modify the breakup and coalescence of drops/bubbles. This could be unphysical, and hence, we set $F_2 = 0$ (hereafter).

Similarly, we can include forcing in the phase-averaged TKE equation, which yields

$$\frac{\partial k_k}{\partial t} = V_k - P_k - \epsilon_k + F_{3,k}. \tag{2.15}$$

While there are many possible forms for the forcing terms F_1 and $F_{3,k}$, it has been shown that a linear forcing term in velocity applied in physical space generates more favorable statistics of third-order structure functions, and presumably other inertial range statistics, as compared with low-wavenumber forcing (Lundgren 2003). Given that we wish to study the breakup and coalescence of droplets in the inertial range of turbulence, this fact, combined with the ease of implementation, leads us to use linear forcing. If we adopt linear forcing of the form $\rho A u_i$ for the mixture momentum equation and $\rho A \phi_k u_i$ for the phase momentum equation, where A is a constant with the units of time, then the forcing terms in the energy equations will be

$$F_1 \equiv A\langle \rho u_i u_i \rangle = 2Ak, \tag{2.16}$$

and

$$F_{3,k} \equiv A\frac{\langle \phi_k \rho_k u_i u_i \rangle}{\langle \phi_k \rangle} = 2Ak_k. \tag{2.17}$$

If we use a controller (Bassenne *et al.* 2016) of the form

$$\frac{\partial q}{\partial t} = T + F + G\left(\frac{q - q_\infty}{t_{l,\infty}}\right), \tag{2.18}$$

then the generic forcing will be of the form

$$F = -T - G\left(\frac{q - q_\infty}{t_{l,\infty}}\right). \tag{2.19}$$

2.3.1. *Constant TKE*

From Eq. (2.13), if we set,

$$F_1 = \epsilon - \Psi, \tag{2.20}$$

then the TKE will be constant in stationary state. To achieve this, we need

$$A = \frac{\epsilon - \Psi}{2k}, \tag{2.21}$$

or with the controller,

$$A = \frac{\epsilon - \Psi - G\left(\frac{k-k_\infty}{t_{l,\infty}}\right)}{2k}, \tag{2.22}$$

2.3.2. *Constant total energy*

From Eq. (2.14), if we set

$$F_1 = \epsilon, \tag{2.23}$$

then the total energy (TE) = TKE + SE will be constant in stationary state. To achieve this, we need

$$A = \frac{\epsilon}{2k}, \tag{2.24}$$

or with the controller,

$$A = \frac{\epsilon - G\left(\frac{k+se-k_\infty-se_\infty}{t_{l,\infty}}\right)}{2k}. \tag{2.25}$$

2.3.3. *Constant individual phase TKE*

From Eq. (2.15), if we set

$$F_{3,k} = \epsilon_k + P_k - V_k, \tag{2.26}$$

then the phase TKE will be constant in stationary state. To achieve this, we need

$$A = \frac{\epsilon_k + P_k - V_k}{2k_k}, \tag{2.27}$$

or with the controller,

$$A = \frac{\epsilon_k + P_k - V_k - G\left(\frac{k_k-k_{k,\infty}}{t_{l,\infty}}\right)}{2k_k}. \tag{2.28}$$

The effect of holding each of these energy choices constant in the subsequent simulations is examined. Figure 2 also shows the energy injection points in the schematic.

2.4. *Computational setup*

For all cases presented in this study, the computational setup consists of a triply periodic domain of size $(2\pi)^3$ discretized using N^3 points with $N = 256$. First, a single-phase flow is forced using the controlled forcing in Eq. (2.22) with $\Psi = 0$, such that the final Taylor microscale–based Reynolds number, Re_λ, achieved is $Re_\lambda \approx 87$. This corresponds to a local average resolution of the Kolmogorov length scale, η, of $k_{max}\eta = 1.5$, where k_{max} is the largest wavenumber resolved by the grid, consistent with the direct numerical simulation of single-phase flow reported in Bassenne *et al.* (2016). This process takes around $30\tau_e$ to complete, where τ_e is the large eddy turnover time.

The final stationary single-phase HIT state (Figure 3) is used to initialize all the two-phase HIT simulations. This is done by inserting a second phase sphere (either droplet

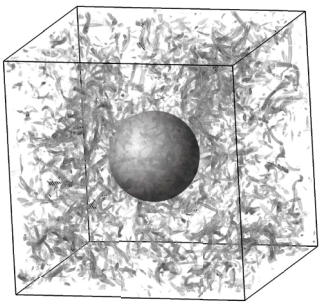

FIGURE 3. Volume rendering of enstrophy of the HIT along with the interface, showing the initial condition for the two-phase simulations.

or bubble) in the center of the domain of diameter $L_d = 1$. To completely disregard the effect of the initialized velocity field inside the second phase, we run this setup using the various controlled forcings until the global surface area of the interface reaches a steady state, after which we collect statistics and make the findings reported below.

Using this setup, we run a variety of cases to test the effect of varying non-dimensional parameters such as the density ratio, ρ_1/ρ_2, the viscosity ratio, μ_1/μ_2, the average void fraction of the dispersed phase, $\langle\phi_d\rangle$, and the integral scale Weber number of the flow defined as $We_l = (2/3)\rho_c u_l^2 l_e/\sigma$. Here, ρ_c is the carrier phase density, l_e is the integral length scale of the single-phase flow defined as $l_e = k_e^{3/2}/\epsilon$, where k_e and ϵ are the targeted kinetic energy and dissipation of the HIT, respectively, and u_l is the RMS velocity of the single-phase turbulence before the insertion of the bubble, which is related to the kinetic energy through $k_e = 3/2u_l^2$. Table 1 reports all the properties used for all cases examined in this study. Case A is the base case from which variations in non-dimensional parameters are studied, and all subsequent plots include case A as a reference point along with the corresponding numbered cases for each parameter variation.

3. Results

3.1. *Effect of different forcing types*

For base case A, which has unity-density and unity-viscosity ratios, low void fraction, and a high We_l, promoting breakup, we test all three possible forcings, Eqs. (2.22), (2.25), (2.28), i.e., holding TKE constant, holding TKE + SE constant, and holding only the TKE of the carrier phase constant, respectively. Figure 4 shows that the control schemes work at maintaining constant kinetic and total energies. However, the net effect on the final SE for the different forcing types is minimal. Hence, for the remainder of the study, we limit ourselves to constant TKE forcing of either a single phase or both phases simultaneously.

3.2. *Effect of void fraction*

While maintaining unity density and viscosity ratios, we first quantify how the energy is distributed between the two phases when they are simultaneously forced as $\langle\phi_d\rangle$ increases from a small value to approximately 0.5, reaching a symmetric binary system.

Case	ρ_1	ρ_2	ρ_1/ρ_2	μ_1	μ_2	μ_1/μ_2	$\langle\phi_1\rangle$	$\langle\phi_d\rangle$	σ	We_l
A	1	1	1	2.0334×10^{-3}	2.0334×10^{-3}	1	0.0655	0.0655	0.079	19.5
Void fraction variation										
B1	1	1	1	2.0334×10^{-3}	2.0334×10^{-3}	1	0.221	0.221	0.079	19.5
B2	1	1	1	2.0334×10^{-3}	2.0334×10^{-3}	1	0.524	0.476	0.079	19.5
B3	1	1	1	2.0334×10^{-3}	2.0334×10^{-3}	1	0.738	0.262	0.079	19.5
Weber number variation										
C1	1	1	1	2.0334×10^{-3}	2.0334×10^{-3}	1	0.0655	0.0655	0.158	9.75
C2	1	1	1	2.0334×10^{-3}	2.0334×10^{-3}	1	0.0655	0.0655	0.79	1.95
Density ratio variation										
D1	1	10^{-2}	100	2.0334×10^{-3}	2.0334×10^{-3}	1	0.0655	0.0655	0.079	19.5
D2	1	10^{-1}	10	2.0334×10^{-3}	2.0334×10^{-3}	1	0.0655	0.0655	0.079	19.5
D3	1	10^{1}	0.1	2.0334×10^{-3}	2.0334×10^{-3}	1	0.0655	0.0655	0.079	19.5
D4	1	10^{2}	0.01	2.0334×10^{-3}	2.0334×10^{-3}	1	0.0655	0.0655	0.079	19.5

TABLE 1. The properties used for all cases examined in this study: the density of each phase, $\rho_{1,2}$, along with their ratio, ρ_1/ρ_2, the viscosity of each phase, $\mu_{1,2}$, along with their ratio μ_1/μ_2, the average volume fraction of phase 1, $\langle\phi_1\rangle$, along with the dispersed phase volume fraction, $\langle\phi_d\rangle$, the surface tension coefficient, σ, and the large-scale Weber number, We_l.

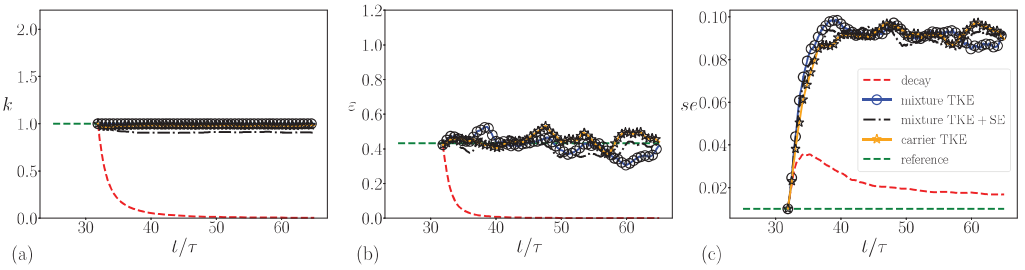

FIGURE 4. Effect of different forcing schemes on the stationary state of case A, showing (a) mixture TKE, (b) mixture dissipation, and (c) SE. The legend applies to all the plots.

Figure 5 showcases the variation of the specific TKE of each phase, $\overline{k_s}$. Since $\rho_1/\rho_2 = 1$ and $\mu_1/\mu_2 = 1$, and both phases are forced, we would expect $\overline{k_s}$ to be 1 (same) for both phases, but we see that the specific kinetic energy in the dispersed phase is less than in the carrier phase. We *hypothesize* that this difference could be due to the *confining effect of the interface, which acts as a soft wall on the dispersed phase and inhibits the formation of large-scale eddies (turbulent fluctuations larger than the drop/bubble size).*

We also find that the specific kinetic energy of the dispersed phase increases approximately linearly with the increase in void fraction, reaching that of the "carrier" phase as $\langle\phi_d\rangle \to 0.5$, since there is no longer a distinction between the two phases of the emulsion at $\langle\phi_d\rangle = 0.5$. This is probably because of the increase in the size of bubbles/drops as the void fraction of the dispersed phase increases. Larger bubbles/drops can now accommodate larger eddies, which is consistent with our hypothesis.

By increasing the void fraction of phase 1 past 0.5 (case B3 in Table 1), we find that the roles of the two phases (phase 1 and phase 2) reverse and the specific kinetic

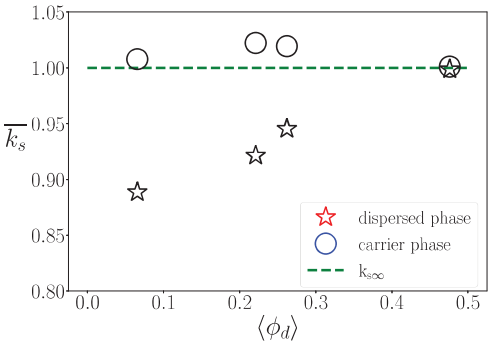

FIGURE 5. Effect of the void fraction on the specific TKE of the dispersed and carrier phases for simultaneous mixture constant TKE forcing. The dashed line represents the reference single-phase value.

energy of the original carrier phase decreases because it now becomes a dispersed phase, highlighting the inhibition of the turbulent fluctuations within the dispersed phase due to the interaction with the "soft wall" behavior of the interface.

We can further attempt to verify this claim by computing the phase-dependent TKE spectra utilizing a filtering approach (Sadek & Aluie 2018). Note that a standard Fourier spectrum, while valid in the present case, is not a general enough approach for when there are variations in density and viscosity between the two phases due to the discontinuity of the velocity derivatives at the interface. Figure 6 showcases the filtering spectrum in both the carrier and dispersed phases. For the dispersed phase, there are two peaks, a high and a low wavenumber one, which approach each other as the volume fraction is increased, culminating with a spectrum that is similar to that of the carrier phase at the largest $\langle\phi_d\rangle$. It is speculated that the two peaks at low $\langle\phi_d\rangle$ correspond to the two internal modes of energy within the dispersed phase, i.e., turbulence within the dispersed phase at the small scales and the translational energy of the dispersed cloud at the large scales, [the presence of translational motion of drops was also postulated before by Dodd & Ferrante (2016)]. Efforts to disambiguate the two are currently in progress. However, we can observe that the energy content in the large scales is increasing with increase in $\langle\phi_d\rangle$, which could be due to the presence of larger eddies that can now be accommodated within the drops/bubbles in the dispersed phase, as they grow in size with increase in $\langle\phi_d\rangle$. This observation again corroborates our hypothesis.

Figure 7 showcases the variation of the total surface energy of the emulsion as a function of $\langle\phi_d\rangle$. It can be seen that it increases approximately as $SE \sim \langle\phi_d\rangle^{2/3}$. This can be easily argued from $\langle\phi_d\rangle \sim \ell^3$, where ℓ is an average length scale of the diameter of the dispersed phase, and $\langle A\rangle \sim SE \sim \ell^2$, where $\langle A\rangle$ is the average surface area of the dispersed phase.

3.3. *Effect of Weber number*

Figure 8 showcases that, while holding $\langle\phi_d\rangle$ constant, decreasing the Weber number decreases the specific kinetic energy of the dispersed phase. This could be a result of two possible effects. Firstly, the increased resiliency of the interface to deformation inhibits the formation of larger eddies (turbulent fluctuations) inside the dispersed phase (our hypothesis outlined above), and secondly, the reduction in deformation can lead to a reduction in the number of smaller bubbles formation, reducing the amount of energy that goes into the translational modes of the dispersed phase cloud. One of these factors

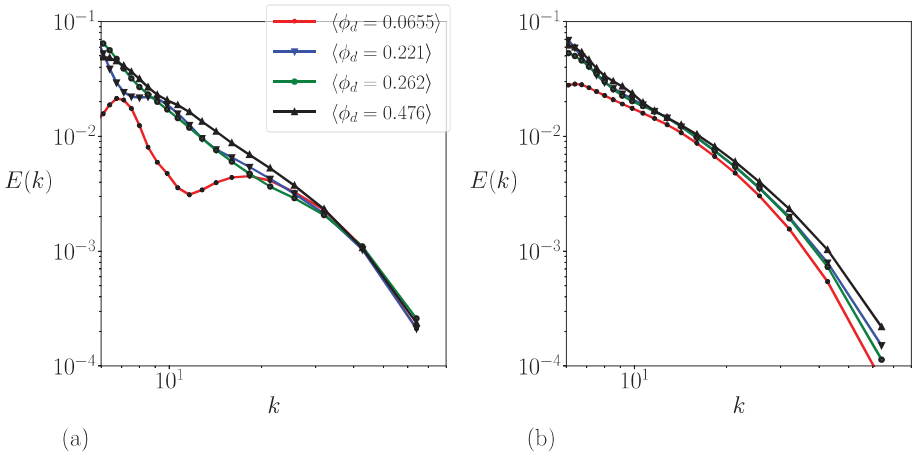

FIGURE 6. The filtering energy spectrum of the (a) dispersed and (b) carrier phases of the emulsion for various void fractions. The legend applies to both plots.

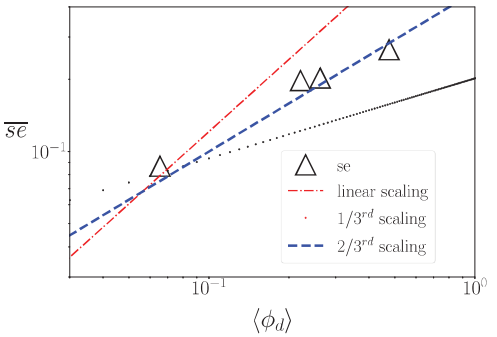

FIGURE 7. Effect of the void fraction on the surface energy of the mixture for simultaneous constant TKE forcing.

could be dominant, or it could be both factors that are at play and are responsible for the reduction in the specific kinetic energy of the dispersed phase. However, we verify that reduction in Weber number with respect to the base case A, reduces the number of sub-Hinze scale bubbles in the stationary size distribution of the dispersed cloud, as seen in Figure 9, due to reduced breakup at lower Weber numbers.

3.4. *Effect of density ratio*

We now examine the final steady state reached by a two-phase turbulent system as the dispersed phase changes from low-density bubbles to emulsions to high-density droplets. Figure 10(a) shows that if we force both phases simultaneously, a large variation in the energy distribution of the two phases does not exist until we transition to droplets. In that case, simultaneously forcing both cases dumps a lot of kinetic energy into the droplets by virtue of their increased density, while draining the carrier phase considerably. This is considered not physically relevant, as the large-scale energy injection mechanisms likely act on the carrier phase in cases of interest, so we proceed to individually hold the kinetic energy of the carrier phase constant as we vary the density ratio. Figure 10(b) shows that while holding the carrier phase TKE constant, there is a stark difference between

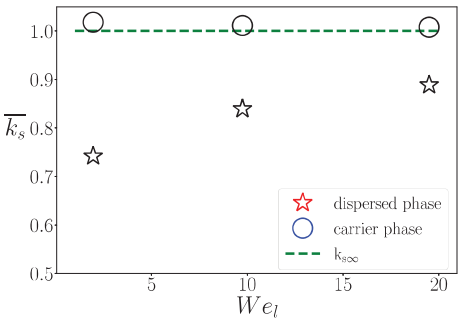

FIGURE 8. The specific TKE of each phase as a function of Weber number. The dashed line represents the reference single-phase value.

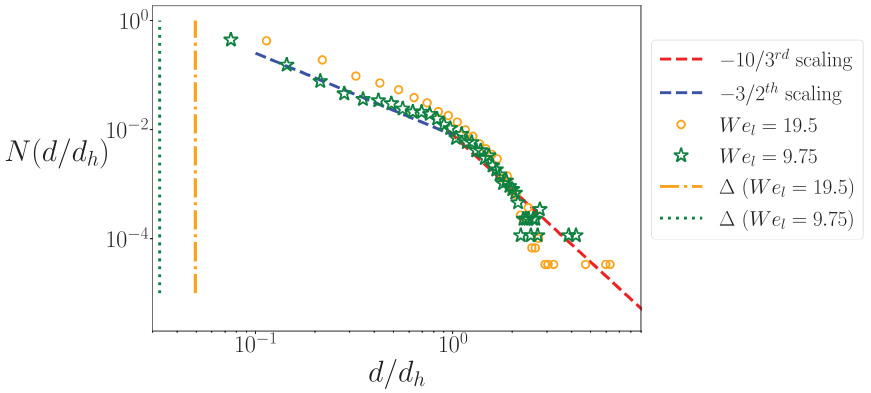

FIGURE 9. Effect of Weber number on the size distribution of the dispersed phase. The vertical lines represent grid sizes.

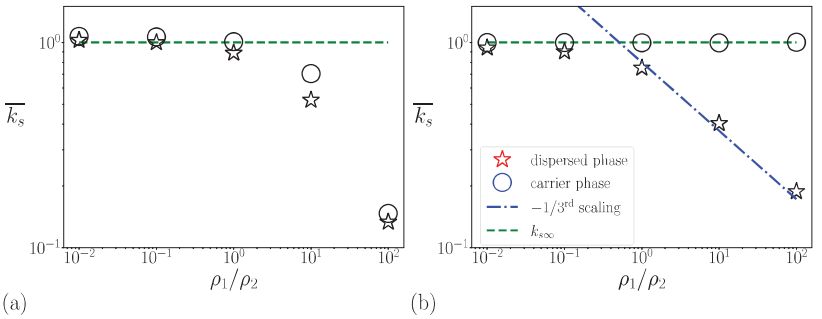

FIGURE 10. Effect of density ratio on the specific TKE of the phases for (a) constant mixture-TKE forcing, (b) constant carrier phase TKE forcing. The dashed line represents the reference single-phase value.

the behavior of bubbles and droplets. For bubbles, their specific kinetic energy is roughly constant across two orders of magnitude. However, as soon as the dispersed phase changes to droplets, its specific kinetic energy decays following at $KE_d \sim (\rho_1/\rho_2)^{-1/3}$ power-law. This is likely due to the transition from storing energy in internal modes (in bubbles) to translational modes (in drops).

4. Summary and conclusions

In this work, we performed forced numerical simulations of two-phase homogeneous isotropic turbulence and studied the statistical behavior of two-phase turbulent mixture. We performed simulations for various density ratios (representing bubbles, drops, and emulsions), Weber number, and void fraction and studied the effect of these parameters on the global behavior of the two-phase mixture. We also formulated various forcing schemes, including mixture-phase (both phases) forcing and single-phase (carrier) forcing, that can hold the turbulent kinetic energy of the mixture or the carrier phase a constant value in steady state.

In this study, we found that the interface behaves as a "soft wall" and inhibits formation of larger eddies (turbulent fluctuations) within the dispersed phase. This hypothesis was developed by looking at the specific turbulent kinetic energy variation as a function of void fraction and Weber number. The specific turbulent kinetic energy in the dispersed phase increased with increase in void fraction and Weber number, indicating that larger eddies can be accommodated in larger bubbles/drops and when the interface is more deformable, respectively. Furthermore, the energy spectrum in the dispersed phase showed increased energy at larger scales as void fraction increased, verifying that the interface could be blocking the formation of larger eddies.

We also observed and explained that the global surface energy of the two-phase mixture scales as a $2/3^{rd}$ power-law of void fraction. Moreover, we found that the specific kinetic energy follows a $-1/3^{rd}$ power-law of the density ratio for droplets (heavier dispersed phase) and is independent of the density ratio for bubbles (lighter dispersed phase). This interesting observation demonstrates that drops behave fundamentally differently from bubbles. Overall, this study has significant implications for subgrid-scale modeling for two-phase turbulent flows.

Acknowledgments

S. S. J. acknowledges financial support from Boeing Co. A. E. acknowledges financial support from NASA Transformational Tools and Technologies grant #80NSSC20M0201. The authors also acknowledge discussions with Parviz Moin.

REFERENCES

Bassenne, M., Urzay, J., Park, G. I. & Moin, P. 2016 Constant-energetics physical-space forcing methods for improved convergence to homogeneous-isotropic turbulence with application to particle-laden flows. *Phys. Fluids* **28**, 035114.

Begemann, A. , Trummler, T., Traunter, E., Hasslberger, J. & Klein, M. 2022 Effect of turbulence intensity and surface tension on the emulsification process and its stationary state—a numerical study. *Can. J. Chem. Eng.* **100**, 3548–3561.

Brackbill, J. U., Kothe, D. B. & Zemach, C. 1992 A continuum method for modeling surface tension. *J. Comp. Phys.* **100**, 335–354.

Brown, L., Jain, S. S. & Moin, P. 2023 A phase field model for simulating the freezing of supercooled liquid droplets. *SAE Technical Paper*, 2023-01-1454.

Collis, H., Mirjalili, S., Jain, S. S., & Mani, A. 2022 Assessment of WENO and TENO schemes for the four-equation compressible two-phase flow model with regularization term. *Annual Research Briefs*, Center for Turbulence Research, Stanford University, pp. 151–165.

Crialesi-Esposito, M., Chibbaro, S. & Brandt, L. 2023 The interaction of droplet dynamics and turbulence cascade. *Comm. Phys.* **6**, 1.

Crialesi-Esposito, M., Rosti, M. E., Chibbaro, S. & Brandt, L. 2022 Modulation of homogeneous and isotropic turbulence in emulsions. *J. Fluid Mech.* **940**, A19.

Dieke, L. 2022 Mass transfer at the ocean-atmosphere interface: the role of wave breaking, droplets, and bubbles. *Annu. Rev. Fluid Mech.* **54**, 191–224.

Dodd, M. S. & Ferrante, A. 2016 On the interaction of Taylor length scale size droplets and isotropic turbulence. *J. Fluid Mech.* **806**, 356–412.

Farsoiya, P. K., Liu, Z., Daiss, A., Fox, R. O. & Dieke, L. 2023 Role of viscosity in turbulent drop breakup. *J. Fluid Mech.* **972**, A11.

Grabowski, W. W. & Wang, L. P. 2013 Growth of cloud droplets in a turbulent environment. *Annu. Rev. Fluid Mech.* **45**, 293–324.

Hwang, H. & Jain, S. S. 2023 A robust phase-field method for two-phase flows on unstructured grids. *arXiv Preprint* arXiv:2310.10795.

Jain, S. S. 2017 Flow-induced breakup of drops and bubbles. *arXiv Preprint* arXiv:1701.06157.

Jain, S. S. 2022 Accurate conservative phase-field method for simulation of two-phase flows. *J. Comp. Phys.* **469**, 111529.

Jain, S. S. 2023 A model for transport of interface-confined scalars and insoluble surfactants in two-phase flows. *arXiv Preprint* arXiv:2311.11076.

Jain, S. S. & Moin, P. 2022 A kinetic-energy and entropy-preserving scheme for compressible two-phase flows. *J. Comp. Phys.* **464**, 111307.

Kilpatrick, P. K. 2012 Water-in-crude oil emulsion stabilization: review and unanswered questions. *Energy & Fuels* **26**, 4017–4026.

Krzeczek, O. Trummler, T., Traunter, E. & Klein, M. 2023 Effect of density ratio on emulsions and their segregation: A direct numerical simulation study. *Energies* **16**, 3160.

Lundgren, T. S. 2003 Linearly forced isotropic turbulence. *Annual Research Briefs*, Center for Turbulence Research, Stanford University, pp. 461–473.

Ni, R. 2024 Deformation and breakup of bubbles and drops in turbulence. *Annu. Rev. Fluid Mech.* **56**, 319–347.

Perrard, S., Riviére, A., Mostert, W. & Dieke, L. 2021 Bubble deformation by a turbulent flow. *J. Fluid Mech.* **920**, A15.

Riviére, A., Mostert, W., Perrard, S. & Dieke, L. 2021 Sub-Hinze scale bubble production in turbulent bubble breakup. *J. Fluid Mech.* **917**, A40.

Riviére, A., Ruth, D. J., Mostert, W., Dieke, L. & Perrard, S. 2022 Capillary driven fragmentation of large gas bubbles in turbulence. *Phys. Rev. Fluids* **7**, 083602.

Rosales, C. & Meneveau, C. 2005 Linear forcing in numerical simulations of isotropic turbulence: physical space implementations and convergence properties. *Phys. Fluids* **17**, 095106.

Sadek, M. & Aluie, H. 2018 Extracting spectrum of a flow by spatial filtering. *Phys. Rev. Fluids* **3**, 124610.

Scapin, N., Shahmardi, A., Chan, W. H. R., Jain, S. S., Mirjalili, S., Pelanti, M., Brandt, L. 2022 A mass-conserving pressure-based method for two-phase flows with phase change. *Proceedings of the Summer Program*, Center for Turbulence Research, Stanford University, pp. 195–204.

Trgyyvason, G., Scardovelli, R. & Zaleski, S. 2011 *Direct Numerical Simulations of Gas–Liquid Multiphase Flows*. Cambridge University Press

Vela-Martín, A. & Avila, M. 2021 Deformation of drops by outer eddies in turbulence. *J. Fluid Mech.* **929**, A38.

Vela-Martín, A. & Avila, M. 2022 Memoryless drop breakup in turbulence. *Sci. Adv.* **8**, eabp9561.

Wang, L., Li, X., Zhang, G., Dong, J. & Eastoe, J. 2007 Oil-in-water nanoemulsions for pesticide formulations. *J. Colloid & Int. Sci.* **314**, 230–235.